Journal of Quantitative Spectroscopy & Radiative Transfer 124 (2013) 62–78

Contents lists available at SciVerse ScienceDirect

Journal of Quantitative Spectroscopy & Radiative Transfer

journal homepage: www.elsevier.com/locate/jqsrt

Experimental and simulated scattering matrices of small calcite particles at 647 nm

D.D. Dabrowska [a,*], O. Muñoz [a], F. Moreno [a], T. Nousiainen [b], E. Zubko [b,c], A.C. Marra [d]

[a] Instituto de Astrofísica de Andalucía, CSIC Glorieta de Astronomía s/n, Granada 18008, Spain
[b] Department of Physics, P.O. Box 64, FI-00014, University of Helsinki, Finland
[c] Astronomical Institute of Kharkov National University Kharkov, Ukraine
[d] Institute of Atmospheric Science and Climate, CNR, 73100 Lecce, Italy

ARTICLE INFO

Article history:
Received 27 November 2012
Received in revised form
12 February 2013
Accepted 13 February 2013
Available online 20 February 2013

Keywords:
Calcite
Martian dust analogs
Atmospheric dust
Light scattering
Irregular particles

ABSTRACT

We present measurements of the complete scattering matrix as a function of the scattering angle of a sample of calcite particles. The measurements are performed at 647 nm in the scattering angle range from 3° to 177°. To facilitate the use of the experimental data we present a synthetic scattering matrix based on the measurements and defined in the full range from 0° to 180°. The scattering matrix of the calcite sample is modeled using the discrete-dipole approximation. Two sets of shapes, flake-like and rhomboid-like particles giving a total of 15 different targets are considered since both types of shapes have been found in our calcite sample. In our computations we use the measured size distribution of the calcite sample truncated at 1.2 μm. We present a theoretical study of the impact of birefringence on the computed scattering matrix elements for both sets of shapes. Four different cases regarding the composition of the calcite particles are considered: two isotropic cases corresponding to the ordinary and extraordinary refractive index of calcite, respectively; one equivalent isotropic case analogous to internal mixing; and birefringence fully accounted for. Numerical simulations are compared with the experimental data. We find that birefringence has little impact on the calculated phase functions but it has a significant effect on the polarization-related elements of the scattering matrix. Moreover, we conclude that the shape of the targets (flakes or irregular rhomboids) has a much stronger effect on the computed scattering matrix elements than birefringence.

1. Introduction

The study of light scattering by small particles is of interest for different scientific disciplines, from medicine to astrophysics. Dust grains exist in a wide variety of cosmic environments ranging from the diffuse interstellar medium, molecular clouds, and disks around new stellar objects [1–3], to cometary [4] and planetary atmospheres (e.g. [5–7]). Those dust particles play an important role in the radiative balance and dynamics of the atmosphere. Moreover, small particles can be absorbed by human pulmonary airways causing some diseases such as talcosis or silicosis [8].

In this paper we present measurements of the complete scattering matrix as a function of the scattering angle of a calcite sample. The measurements are performed in the 3–177° scattering angle range at the wavelength of 647 nm. The lack of experimental data at very small and very large scattering angles [0–3°], and [177–180°] limits the use of the experimental data. Therefore, we also present the extrapolated scattering matrix that is defined in the entire angle range from 0° to

* Corresponding author. Tel.: +34 958230505.
E-mail address: dominika@iaa.es (D.D. Dabrowska).

0022-4073/$ - see front matter © 2013 Elsevier Ltd. All rights reserved.
http://dx.doi.org/10.1016/j.jqsrt.2013.02.010

180° [9]. The extrapolation of the phase function is performed using the procedure suggested by Liu et al. [10] and subsequently adopted by, e.g., Kahnert and Nousiainen [11] and Muñoz et al. [9].

Although calcite is not a major component of the Martian surface, it is commonly considered to be particularly important for its link with climate evolution and water resources on Mars [12,13]. Moreover, calcite is also found in the Earth's atmosphere. Desert dust is rich in calcite [14,15], the Saharan desert being one of the main sources of mineral dust in our atmosphere [6].

In addition to its relevance for atmospheric applications, calcite is also very interesting from the light scattering modeling point of view due to its high birefringence. In this work we use the DDSCAT 7.1 code [16] to perform a theoretical study of the impact of birefringence on the computed scattering matrix elements. The computations are compared with the experimentally determined scattering matrix for the calcite sample. A detailed physical characterization of our sample is presented in Section 2. In Section 3, we describe the experimental apparatus used in this work together with the experimental scattering matrix of our calcite sample. Simulations of the scattering matrix elements as functions of the scattering angle are discussed in Section 4. Summary and conclusions are given in Section 5.

2. The calcite sample

2.1. Origin of the calcite sample and size distribution

The calcite sample is obtained from a limestone bulk sample collected near Lecce, Italy [17]. Limestone is a very abundant mineral on the Earth, calcite being its main component (98%). We ground the bulk limestone sample with an Agatha ball-miller to obtain fine powder. The size distribution of the resulting sample is measured using a Mastersizer 2000 from Malvern Instruments. The Mastersizer measures the phase function of the sample at 633 nm in a certain scattering-angle range with special attention to the forward diffraction region. Subsequently, it uses either Lorenz–Mie or Fraunhofer diffraction theory to retrieve the volume distribution that best fits the measurements. It is important to note that the retrievals from both methods are simplifications based on the assumption that the particles are spherical (see [18]). Further studies are required to clarify which SD is more representative for our samples of irregular particles. Accordingly, we present the size distributions based on both Fraunhofer and Lorenz–Mie theories so that the reader can choose which one is more appropriate for his/her purposes or take the average.

In Fig. 1, we plot the number $n(r)$, projected-surface-area $S(\log r)$ and volume $V(\log r)$ distributions for the calcite sample retrieved from both, the Fraunhofer and Lorenz–Mie theories. Here, r represents the radius of a sphere having the same volume as the particle (volume-equivalent sphere). The transformation equations to obtain $n(r)$, $S(\log r)$ and $V(\log r)$ from the measured $v(r)$ are given in the Amsterdam–Granada Light Scattering Database http://www.iaa.es/scattering/site_media/sizedistributions.pdf (see also [19]). In the database [20] we present tables of $N(\log r)$, $S(\log r)$ and $V(\log r)$, as well as the corresponding $n(r)$, $s(r)$ and $v(r)$ based on both the Fraunhofer and Lorenz–Mie theories. As can be seen from Fig. 1, the use of Lorenz–Mie theory in the size retrieval results in larger particle sizes than the Fraunhofer theory. This can be seen for $V(\log r)$ and $S(\log r)$, but is especially pronounced in $n(r)$. Interestingly, the Fraunhofer retrieval results in a bimodal $V(\log r)$ the small-particle mode being less prominent in the Mie-based retrieval. This bi-modality may be an artifact. From the measured size distributions we also calculate the values of the effective radius r_{eff} and effective variance v_{eff} as defined by Hansen and Travis [21],

$$r_{eff} = \frac{\int_0^\infty r\pi r^2 n(r)\,dr}{\int_0^\infty \pi r^2 n(r)\,dr}, \tag{1}$$

$$v_{eff} = \frac{\int_0^\infty (r-r_{eff})^2 \pi r^2 n(r)\,dr}{r_{eff}^2 \int_0^\infty \pi r^2 n(r)\,dr}. \tag{2}$$

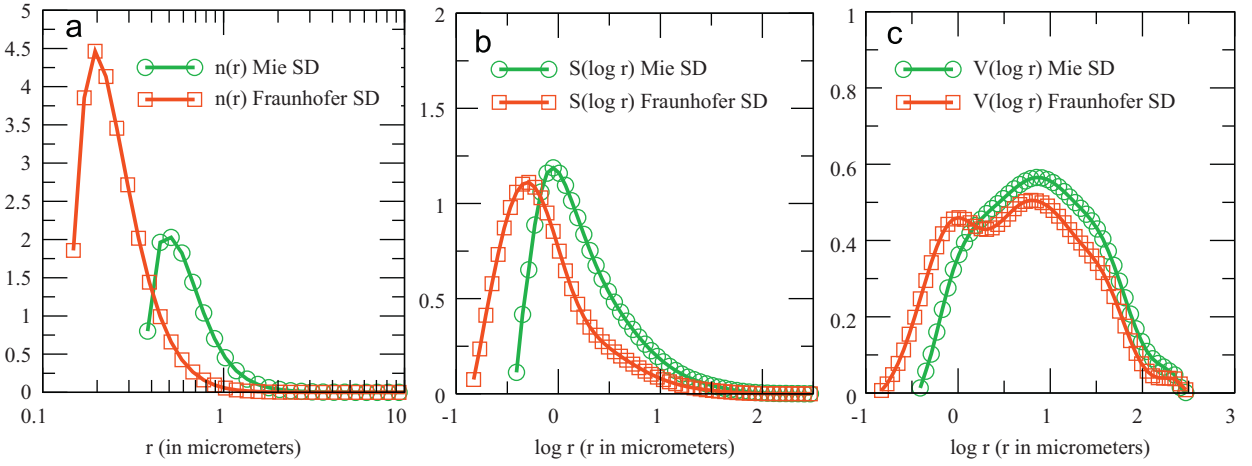

Fig. 1. (a) Normalized number, (b) projected-surface-area and (c) volume distributions of the calcite sample as a function of r and $\log r$ as measured by a Mastersizer 2000 from Malvern Instruments, based on using either Fraunhofer and Lorenz–Mie theories.

The resulting values for the calcite sample are presented in Table 1.

2.2. Refractive index

Calcite is a uni-axial birefringent material, so it has one optic axis and, instead of one refractive index, it has a dielectric tensor specified by two principal dielectric functions, the ordinary and the extraordinary refractive indices. These refractive indices are dependent on the wavelength, the real part of the ordinary refractive index, n_o, varying roughly between 1.57 and 1.47, while the extraordinary refractive index, n_e, varies between 1.88 and 1.62 in the 0.2−3.3 μm wavelength range [22]. At the wavelength of the measurements and simulations, 647 nm, $n_o=1.655$ and $n_e=1.485$ [22]. The imaginary part of the refractive index, k, is assumed to be zero since pure calcite is very weakly absorbed in the visible region.

Table 1
The effective radii r_{eff} and effective variances v_{eff} retrieved from the Fraunhofer and Lorenz–Mie size distributions.

Method	r_{eff} (μm)	v_{eff}
Fraunhofer	1.7	7.6
Lorenz–Mie	3.3	4.9

2.3. Shapes

In Fig. 2, we show Field Emission Scanning Electron Microscope (FESEM; top panels), and Scanning Electron Microscope (SEM; bottom panels) images arbitrarily chosen to show the shape of our calcite particles. It should be noted that the microscope images are not necessarily representative of the size distribution (for that purpose, we refer the reader to Fig. 1). As mentioned, the original sample is ball-milled to produce smaller particles. After this artificial procedure, two kinds of shapes are found. In addition to the typical flake-like shapes of calcite particles, many rhomboidal structures are also present (Fig. 2, bottom panels). Both types of shapes have also been found in natural samples [15].

3. Experimental data

3.1. Experimental apparatus

The flux and state of polarization of a beam of quasi-monochromatic light can be described by means of a so-called flux vector. If such a beam of light is scattered by a sample of randomly oriented particles with equal amounts of particles and their mirror particles, the flux vectors of the incident beam, $\pi\mathbf{\Phi_0}$, and scattered beam, $\pi\mathbf{\Phi_{det}}$, are related by the 4×4 scattering matrix, $\mathbf{F}$, for

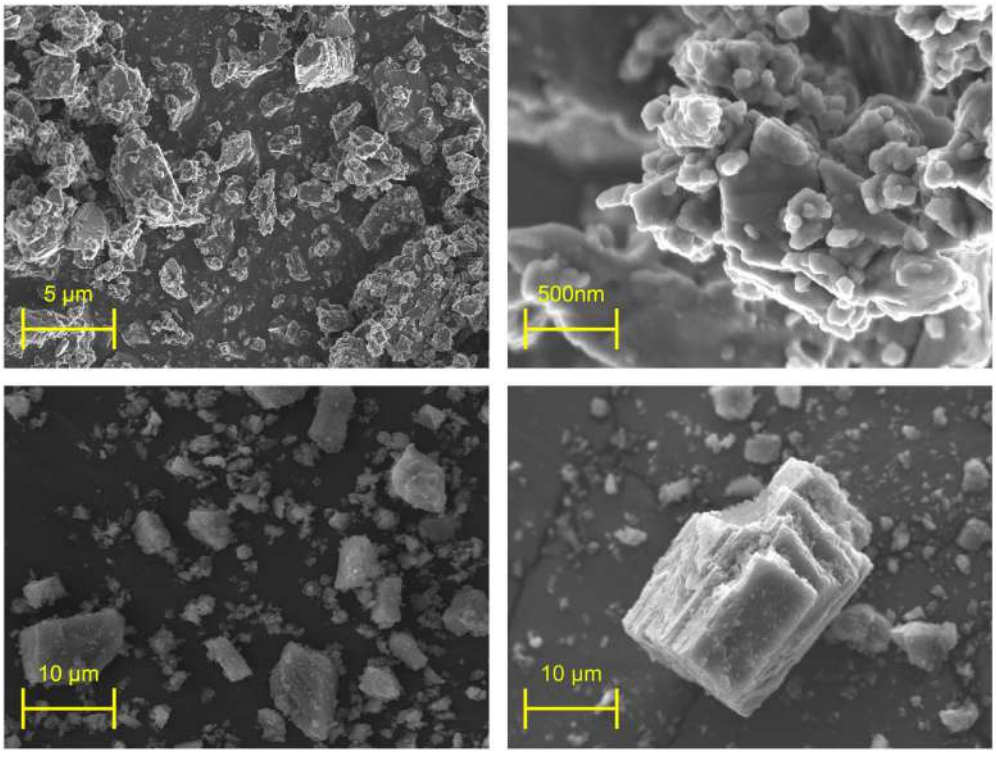

Fig. 2. Top panels: FESEM images of the calcite sample. Bottom: SEM images of the calcite sample. The bars at the left bottom corners denote the scale of the images. Note that the scale bars differ among panels.

each scattering angle θ, as follows [23,24]:

$$\mathbf{\Phi_{det}}(\lambda,\theta) = \frac{\lambda^2}{4\pi^2 D^2} \begin{pmatrix} F_{11} & F_{12} & 0 & 0 \\ F_{12} & F_{22} & 0 & 0 \\ 0 & 0 & F_{33} & F_{34} \\ 0 & 0 & -F_{34} & F_{44} \end{pmatrix} \mathbf{\Phi_0}(\lambda), \qquad (3)$$

where the first elements of the column vectors are fluxes divided by π and the other elements describe the state of polarization of the beams by means of Stokes parameters. Furthermore, λ is the wavelength, and D is the distance from the sample to the detector. The matrix $\mathbf{F}$ with elements $F_{i,j}$ is called the scattering matrix of the sample and refers to light that has been scattered once. The elements of the scattering matrix are dimensionless and depend on the physical properties of the particles (size, shape, and refractive index), the number of the scattering particles that contribute to the detected radiation, the wavelength of the incident light, and the direction of the scattered light, which, for randomly oriented particles, are sufficiently described by means of the scattering angle θ. The scattering angle, θ, is defined by the directions of the incident and scattered light.

The scattering matrix of our sample of calcite particles is measured at the IAA COsmic DUst LABoratory (CODULAB) [25]. In Fig. 3, we present a photograph of the experimental apparatus. In our experiment we use an Argon–Krypton laser as a light source. It emits linearly polarized light at one of the five possible wavelengths, namely, 483 nm, 488 nm, 520 nm, 568 nm and 647 nm. The light passes through a polarizer and an electro-optic modulator. The light is subsequently scattered by randomly oriented particles located in a jet stream produced by an aerosol generator, so no vessel is needed to contain the sample. This is a big advantage since any object containing the sample may cause undesirable reflections. Subsequently, the scattered light passes through a quarter wave plate, Q, and an analyzer, A, (both optional) and is detected by a photomultiplier tube which moves in steps along a ring around the ensemble of particles, the detector. In this way a range of scattering angles from 3° to 177° is covered in the measurements. All matrix elements (except F_{11} itself) are normalized to F_{11}, that is, we consider F_{ij}/F_{11}, with $i,j=1$–4 with the exception of $i=j=1$. Due to the lack of measurements between 0° and 3° and 177° and 180°, we cannot measure the absolute dependence of the $F_{11}(\theta)$ element. Instead, we normalize the measured $F_{11}(\theta)$ to 1 at 30°. The function $F_{11}(\theta)$, normalized in this way, is called the phase function or scattering function in this paper. Another photomultiplier tube, the monitor, is located in a fixed position and is used to correct for fluctuations in the aerosol cloud. By using eight different combinations of the optical components and their orientations, and assuming the reciprocity of the sample (in particular $F_{21}=F_{12}$, $F_{31}=-F_{13}$ and $F_{41}=F_{14}$), all scattering matrix elements are obtained as functions of the scattering angle [26]. A detailed description of the instrument is given by Muñoz et al. [25].

The reliability of the apparatus has been tested by comparing measured scattering matrices of spherical water droplets at 488 nm, 520 nm and 647 nm with Lorenz–Mie computations [25]. Special tests have been performed to ensure that our experimental results are not significantly contaminated by multiple scattering [18]. In addition, we check that the measured scattering matrices

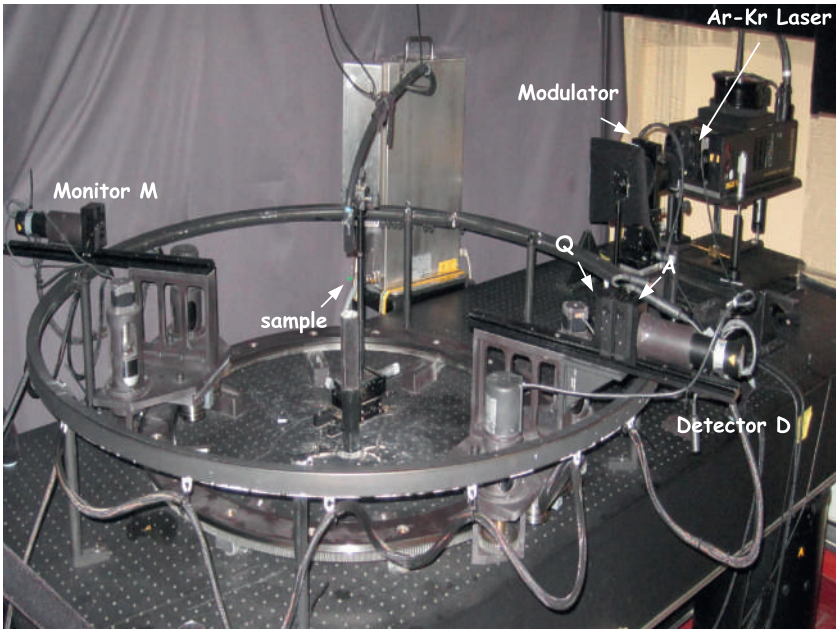

Fig. 3. Photograph of the experimental apparatus. On the right we can see the detector that moves along the ring. The ring is placed horizontally in the laboratory with an outer diameter of 1 m. The monitor is located on the left. In the middle, we see the nozzle of the nebulizer located vertically in the center of the ring and the green spot is where the laser beam interacts with the aerosol cloud. (For interpretation of the references to color in this figure caption, the reader is referred to the web version of this article.)

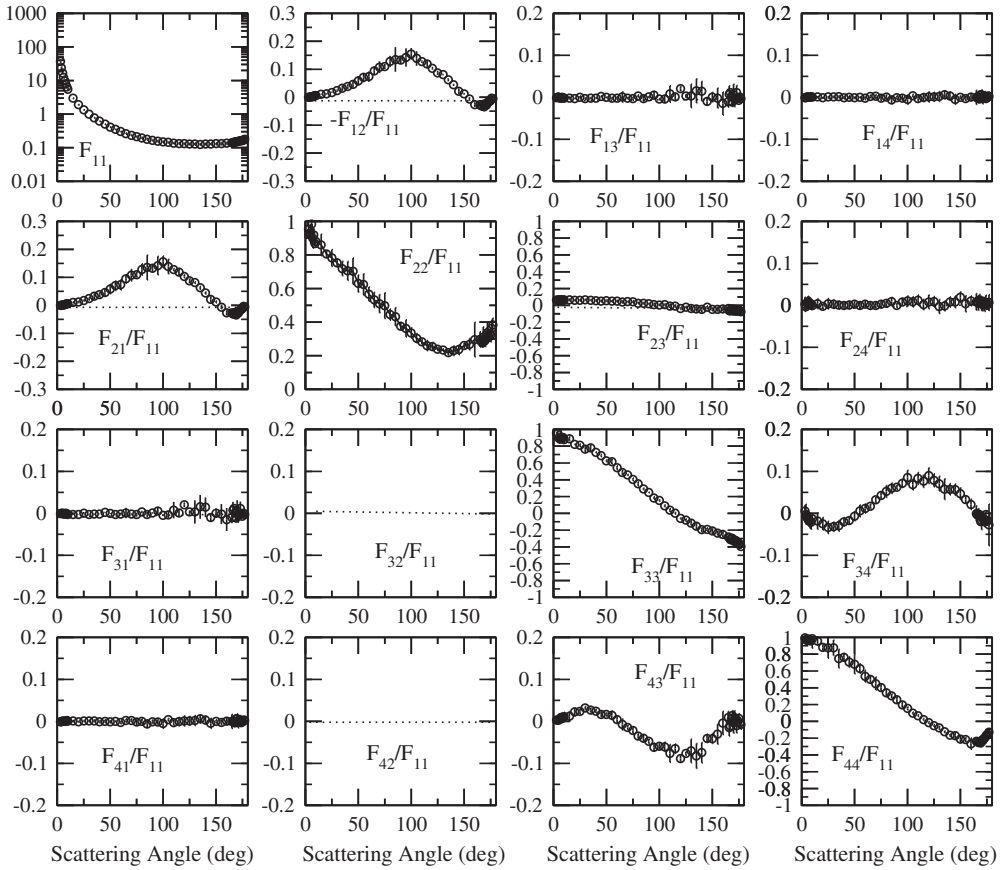

Fig. 4. Measured scattering matrix elements as functions of the scattering angle at 647 nm wavelength. Circles correspond to the measurements that are presented together with their error bars.

fulfill the Cloude coherency matrix test [27] within the experimental errors at all measured scattering angles.

3.2. Experimental scattering matrix

In Fig. 4, we present the measured scattering matrix as a function of the scattering angle for our sample of randomly oriented calcite particles. The measurements have been performed in the scattering angle range 3–177° at a wavelength of 647 nm. As mentioned in Section 3.1, all matrix elements (except F_{11} itself) are normalized to F_{11}. The scattering function or phase function, $F_{11}(\theta)$, is shown on a logarithmic scale and is normalized to 1 at 30°. Due to the limited amount of sample we avoid measuring the $F_{32}(\theta)/F_{11}(\theta)$ and $F_{42}(\theta)/F_{11}(\theta)$ ratios. As shown in Fig. 4, the measured $F_{13}(\theta)/F_{11}(\theta)$, $F_{14}(\theta)/F_{11}(\theta)$ and $F_{24}(\theta)/F_{11}(\theta)$ are zero within the experimental errors in the full scattering angle range i.e., the measured scattering matrix has the form presented in Eq. (3). That is a good indication that the aerosol cloud during the measurements can be considered a macroscopically isotropic medium with mirror symmetry even though strictly speaking the assumption of mirror symmetry is not satisfied in a finite sample. In this case, the $-F_{12}(\theta)/F_{11}(\theta)$ ratio is the degree of linear polarization for incident unpolarized light.

In general, the scattering matrix for the calcite sample looks very typical for irregularly shaped mineral particles. For example, the $F_{11}(\theta)$ has a strong forward peak with almost no structure at side- and back-scattering angles. In addition, a slight increase at backward direction is present. The degree of linear polarization for unpolarized incident light, $-F_{12}(\theta)/F_{11}(\theta)$, shows a typical bell shape with a maximum of about 16% at 100° and a negative branch near back-scattering direction. Moreover, the $F_{44}(\theta)/F_{11}(\theta)$ is larger than the $F_{33}(\theta)/F_{11}(\theta)$ at side and back-scattering angles, whereas the $F_{22}(\theta)/F_{11}(\theta)$ deviates from unity at nearly all measured scattering angles.

3.3. Synthetic scattering matrix for the calcite sample

As mentioned, the experimental data do not cover either the exact forward or the exact backward direction. Therefore, what we obtain is the relative phase function, $F_{11}(\theta)/F_{11}(30^\circ)$ with (see [28])

$$\frac{F_{11}(\theta)}{F_{11}(30^\circ)} = \frac{F_{11}^{au}(\theta)}{F_{11}^{au}(30^\circ)}, \tag{4}$$

where $F_{11}^{au}(\theta)$ is the auxiliary phase function which is normalized so that its average over all directions equals

unity, i.e.,

$$1/2\int_0^{\pi} d\theta \sin\theta F_{11}^{au}(\theta)=1. \quad (5)$$

To facilitate the use of the experimental data we construct a synthetic scattering matrix from our measurements that is defined in the full scattering angle range, from 0 to 180°. The extrapolation of the phase function $F_{11}(\theta)$ is based on the assumption that the forward diffraction peak for randomly oriented particles with moderate aspect ratios mainly depends on the size of the particles ([9,10] and references therein). The procedure consists of scaling the measured phase function until its value at 3° matches the Lorenz–Mie computations for the corresponding projected surface area equivalent spheres. For the Lorenz–Mie computations we use the measured size distribution retrieved from both Fraunhofer and Lorentz–Mie theories (Fig. 1) assuming the calcite particles to have a single effective refractive index $m_{eff}=(n_e^2+n_o^2)/3^{(1/2)}=1.60$ corresponding to the internal mixing of n_e and n_o. The imaginary part of the refractive index is fixed to 0. This is a reasonable assumption, as birefringence does not significantly affect the forward scattering peak [15]. The scaled phase function was then extrapolated to 180° assuming a smooth polynomial extrapolation. Once the scattering function is defined in the complete scattering angle range from 0 to 180°, we check whether our extrapolated phase function fulfills Eq. (5). If this conditions is not met, the measured point at the overlap angle (in this case $\theta=3°$) is iteratively adjusted until the normalization condition is satisfied.

For the other scattering matrix elements, $F_{ij}(\theta)/F_{11}(\theta)$ (where $i,j=1\ldots4$, and $i\neq j\neq1$), a polynomial extrapolation is used for both forward and backward directions, with the constraints at the exact forward and backward directions as given by Hovenier et al. [24]:

$$F_{12}(\theta)/F_{11}(\theta)=F_{34}(\theta)/F_{11}(\theta)=0 \quad (\theta=0°,180°), \quad (6)$$

$$F_{22}(0°)/F_{11}(0°)=F_{33}(0°)/F_{11}(0°), \quad (7)$$

$$1\geq\left|F_{22}(0°)/F_{11}(0°)\right|, \quad (8)$$

$$1\geq\left|F_{44}(0°)/F_{11}(0°)\right|, \quad (9)$$

$$F_{44}(0°)/F_{11}(0°)\geq2\left|F_{22}(0°)/F_{11}(0°)\right|-1, \quad (10)$$

$$F_{22}(180°)/F_{11}(180°)=-F_{33}(180°)/F_{11}(180°), \quad (11)$$

$$1\geq\left|F_{22}(180°)/F_{11}(180°)\right|\geq0, \quad (12)$$

$$F_{44}(180°)/F_{11}(180°)\geq1-2\left|F_{22}(180°)/F_{11}(180°)\right|. \quad (13)$$

In addition we verify that the extrapolated points satisfy the Cloude coherency matrix test as described by Hovenier et al. [27]. In Tables A1 and A2, we present the synthetic scattering matrices for the calcite sample obtained for both the measured size distributions. The experimental data and the corresponding extrapolated matrix are freely available in digital form in the Amsterdam–Granada light scattering database [20].

4. Computations for calcite particles

4.1. DDSCAT 7.1

The DDSCAT 7.1 code is a freely available open-source Fortran-90 software package based on the "Discrete Dipole Approximation" (DDA). It computes scattering and absorption of electromagnetic waves by targets with arbitrary shape and complex refractive index. In particular the DDSCAT 7.1 version allows computations for birefringent particles [16]. The theory of DDA is presented in [29].

In the Discrete Dipole Approximation the target is replaced by an array of points. The points acquire dipole moment in response to the local electric field. The dipoles interact electromagnetically with one another. For the finite array of points the scattering problem is exactly solved. DDA is completely flexible regarding the shape of the target, being limited only by the need to use an inter-dipole separation, d, that must be small compared with (1) the size of the particle and (2) the wavelength of the incident light. Although there is no restriction on the relationship between the wavelength and the target size, in practice small size parameters ($x=2\pi r/\lambda$) are much faster to compute than the large ones. Numerical studies [30] indicate that the second criterion is adequately satisfied for non-spherical targets if $|m|kd<1$, where m is the complex refractive index of the target material $k\equiv2\pi/\lambda$ is the wave number and λ the wavelength of the incident light.

4.2. Simulations of calcite particles

As we have seen in Section 2, the calcite sample presents a broad size distribution with particles from the sub-micrometer scale to hundreds of micrometers in radius. A good accuracy in the computations requires the use of a large amount of dipoles for the largest targets. The number of dipoles is directly related to the computational time that increases very quickly as the number of dipoles (size of the target) increases. For a detailed description and limitations of the code we refer to [16]. Due to this limitation, in our computations we cannot take into account the complete size distributions derived from Fraunhofer and Lorenz–Mie theories (hereafter Fraunhofer SD, and Mie SD, respectively) as presented in Section 2.1. Instead, we have to truncate the size distributions at $r=1.2$ μm. The effective radii, r_{eff}, for the truncated Fraunhofer SD and Mie SD are equal to 0.6 and 0.8 μm, respectively. For the Fraunhofer SD a 74% of the total scattering cross-section of the original distribution is included in the truncated distribution whereas only 55% is included if we use the Mie SD.

Owing to the limited size range we can cover with the simulations, we do not attempt to obtain a perfect fit with the measured scattering matrix elements. Instead, we consider the behavior of the computed scattering matrix elements as a function of particle size, shape, and refractive index. For simplicity, for computations involving size averaging, we use the Fraunhofer SD unless it is otherwise noted. Since we do not know which of the two size

distributions is more accurate, the choice is based on the simple reason that a larger fraction of the Fraunhofer SD can be simulated with our truncated SD. Notwithstanding this, size-averaged computations based on the Mie SD are also reported for comparison (see Section 4.5).

In our computations we only consider orientation-averaged results, the number of orientations used depending on the particle size as shown in Table 2. In order to compare the experimental scattering matrix elements for the calcite sample, all computations presented in this paper have been performed at 647 nm.

As we mention in Section 2, the composition of calcite is defined by a dielectric tensor specified by two principal dielectric functions, ordinary and extraordinary refractive indices. To study the impact of birefringence on the simulations, we have considered four cases regarding the composition of calcite particles:

(1) The particles of the sample are assumed to be composed of an isotropic material with a refractive index $m_1 = 1.655 + 0.0i$, corresponding to the ordinary refractive index of calcite.
(2) The particles of the sample are assumed to be composed of an isotropic material with a refractive index $m_2 = 1.485 + 0.0i$, corresponding to the extraordinary refractive index of calcite.
(3) The particles of the sample are considered to be composed of calcite, but its birefringence is approximated by assuming a mixture of particles in such a way that 1/3 are isotropic particles with refractive index m_2, and 2/3 of the particles with refractive index m_1. This is known as the "1/3–2/3 approximation" [29].
(4) The particles of the sample are considered to be composed of calcite, its birefringence fully accounted for.

Table 2
Number of orientations used in our computations for flakes and rhomboids as a function of volume-equivalent radius.

r (μm)	Orientations
0.10	512
0.15	512
0.20	512
0.25	512
0.30	576
0.35	576
0.40	729
0.45	729
0.60	810
0.65	900
0.75	1485
1.00	1485
1.10	1728
1.20	1728

When fully accounting for the birefringence, one needs to specify the orientation of the optic axes relative to the particle. This is straightforward for regular crystals where different crystal faces can be readily identified, but far from trivial for irregular particles without well-defined faces. It is therefore fortunate that the orientation of the optic axis has much reduced effect when averaging over particle orientation [31] as we do here. Further, the effect depends on the particle shape such that large-aspect-ratio particles show larger effect than the more equi-dimensional particles. This is also fortunate, because the orientation of the optic axis is easier to guess at least for calcite when the particles are very thin [15]. Accordingly, for flakes, we use the orientation suggested by [15] and, for simplicity, use the same orientation also for our irregular rhombohedra. For light-scattering simulations for flake-like particles, we use existing model shapes from [15]. Ten such random flakes are used and their ensemble-averaged light-scattering properties are considered here. The generation of these shapes is described in detail by [15] and is not repeated here. Moreover, five new rhomboid-like shapes have been generated (see Fig. 6). Each irregular rhomboid presented in the figure consists of about 100 000 dipoles. Rhomboid-like structures are generated in a similar way, but starting with an ideal rhomboid. Later, seed cells of calcite and void are randomly located close to the surface of the rhomboid, and all the surface cells are turned into either void or calcite, depending on which type of seed is the closest.

For each of the 15 mentioned shapes, scattering matrix computations for 14 different sizes from 0.1 μm to 1.2 μm have been performed (see Table 2). The DDSCAT uses the time factor $\exp(-i\omega t)$ to define the Stokes parameters, causing the sign of the computed $F_{34}(\theta)/F_{11}(\theta)$ to be opposite to that measured. For consistency, the computed $F_{34}(\theta)/F_{11}(\theta)$ are thus multiplied by -1 in the comparison.

4.3. Flake particles

In our computations, for each flake presented in Fig. 5, we consider the 14 size bins shown in Table 2. The computations are averaged over a sufficient amount of

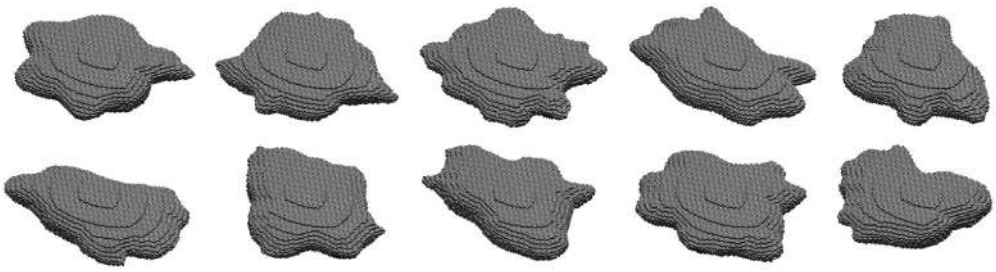

Fig. 5. Modeled flake-like shapes used in our simulations. Each shape consists of about 50 000 dipoles.

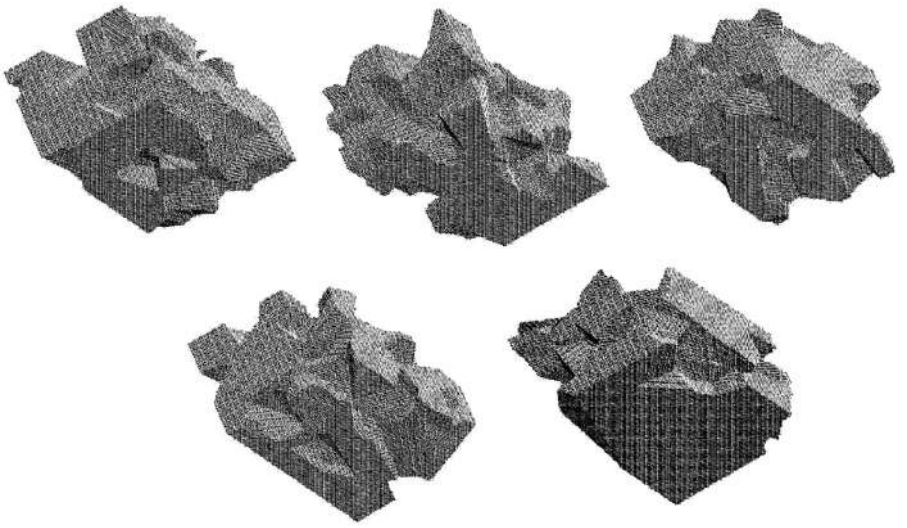

Fig. 6. Modeled rhomboid-like shapes used in our simulations. Each shape consists of about 100 000 dipoles.

orientations to provide a meaningful average (Table 2). Moreover, the simulations for four different compositions as described in Section 4.2 are considered. In practice we only perform computations for three of them, namely, cases 1, 2 and 4, since case 3 is obtained by combining results from 1 and 2. In Fig. 7, we present results for the non-zero elements of the scattering matrix computed for the isotropic case 1 ($m_1=1.655+0.0i$). In the figure, the results for five different sizes, namely, 0.10, 0.45, 0.75, 1.0 and 1.2 μm are displayed, each an average of the 10 shapes. As shown, the computed scattering matrix elements are highly dependent on the size of the particles. As the size increases, some scattering matrix elements, such as the $F_{11}(\theta)$ or $-F_{12}(\theta)/F_{11}(\theta)$ ratio, tend to converge towards the measured values. This is also the case with the $F_{22}(\theta)/F_{11}(\theta)$ and $F_{33}(\theta)/F_{11}(\theta)$ ratios at forward and side scattering angles. A strong dependence of the scattering matrix elements on the particle size is also seen for the other three studied cases referred above regarding the composition. It is good to notice that in some cases the simulations agree well with the measurements already for 1.2 μm particles even though the effective radius of the sample is 1.7 μm containing particles even larger than 200 μm (Fraunhofer SD).

In Fig. 8, we present the scattering matrix elements for the four studied compositions considering averages over all 10 flakes and the Fraunhofer SD truncated at 1.2 μm. As it can be seen, the $F_{11}(\theta)$ element computed for the isotropic case 2 ($m_2=1.485+0i$) substantially differs from the other three cases. Strong differences are also found for the $-F_{12}(\theta)/F_{11}(\theta)$ and $F_{22}(\theta)/F_{11}(\theta)$ ratios when comparing with the results obtained for cases 1, 3 and 4.

The computed phase functions for the isotropic cases 1 ($m_1=1.655+0.0i$) and 3 (1/3–2/3 approximation) are nearly on top of that obtained for the birefringent case 4. Therefore, it seems like birefringence does not significantly affect $F_{11}(\theta)$. However, that is not the case for the polarization-related elements of the scattering matrix. These results are in agreement with the previous studies on the impact of birefringence on the computed scattering matrix elements [15]. When comparing the computed $-F_{12}(\theta)/F_{11}(\theta)$, $F_{22}(\theta)/F_{11}(\theta)$ and $F_{44}(\theta)/F_{11}(\theta)$ ratios for case 3 (1/3–2/3 approximation) with those obtained for the birefringent case 4, we find significant differences at nearly all computed scattering angles. In contrast, the computed $-F_{12}(\theta)/F_{11}(\theta)$ at all scattering angles and the $F_{22}(\theta)/F_{11}(\theta)$ at side- and back-scattering angles for the isotropic case 1 ($m_1=1.655+0.0i$) are very similar to those obtained for the birefringent case 4, constituting a better approximation to the birefringent case than the "1/3–2/3 approximation" as far as the mentioned ratios are concerned.

4.4. Rhomboid-like particles

In analogy with flakes, for each rhomboid-like particle presented in Fig. 6, we consider 14 different sizes as shown in Table 2. The computations are averaged over a sufficient number of orientation in order to provide a meaningful average. Then, the four compositions described in Section 4.2 are considered. In Fig. 9, we show results for the non-zero elements of the scattering matrix computed for the isotropic case 1 ($m_1=1.655+0i$). We present results for five different sizes: 0.10, 0.45, 0.75, 1.00 and 1.20 μm. Each of those sizes has been averaged over the five rhomboid-like particles. We find that the computed scattering matrix elements are highly dependent on the size of the particles. Moreover, a slight increase at the backward direction for the $F_{11}(\theta)$ element appears as the size of the particles increases (particles larger than 0.45 μm). In general, we do not find any clear tendency to approach the measurements for any of the studied sizes. The only exception is found for the $F_{22}(\theta)/F_{11}(\theta)$ and $F_{33}(\theta)/F_{11}(\theta)$ ratios that for the largest radius (1.2 μm) show a reasonable agreement to the measurements. Similar size dependence is found for the other three studied cases regarding the composition referred in Section 4.2.

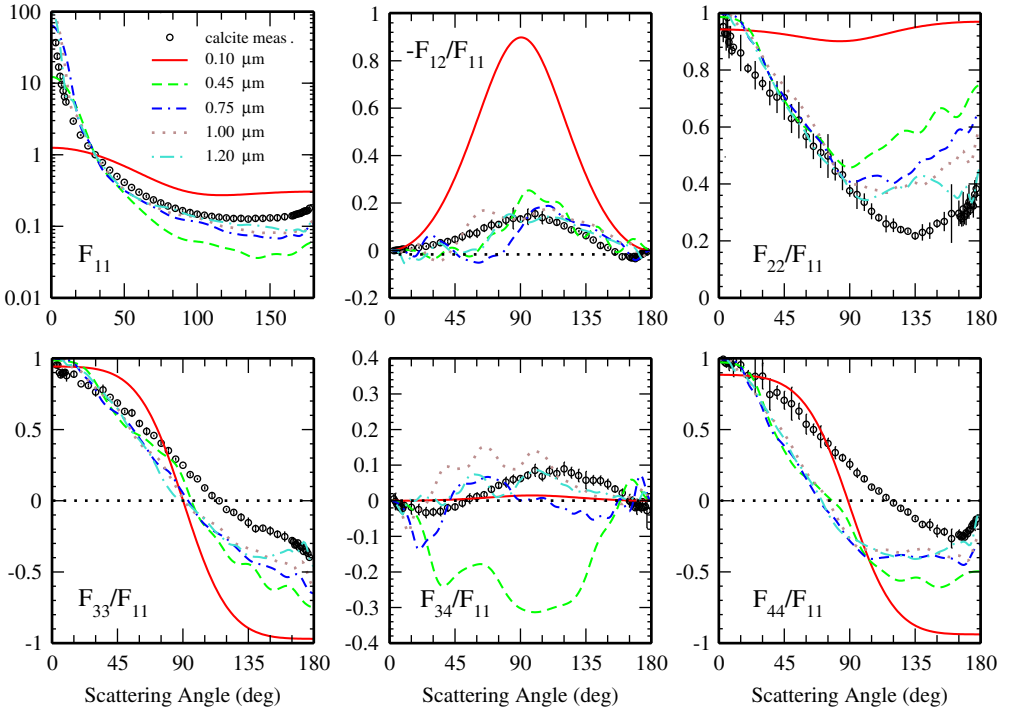

Fig. 7. Computed scattering matrix elements for different volume-equivalent radii. The results are averaged over 10 flake-like shapes fixing the refractive index to $m_1 = 1.655 + 0.0i$. Circles correspond to the measurements that are presented together with their error bars. Computations and measurements have been performed at 647 nm.

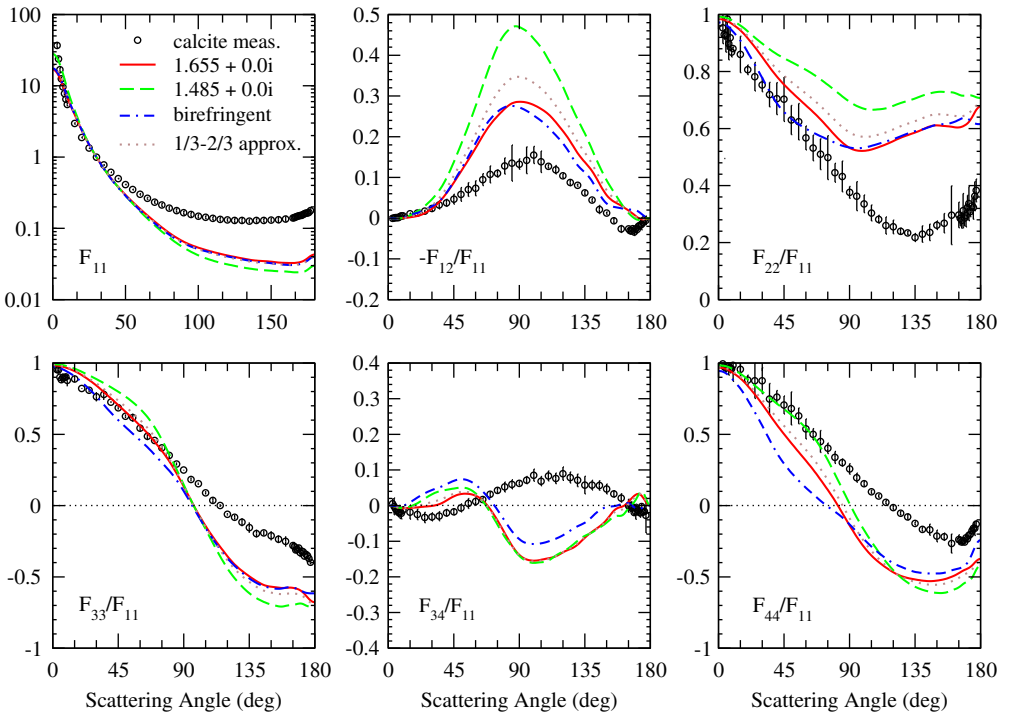

Fig. 8. Computed scattering matrix elements for different refractive indices. The results are averaged over ten flake-like shapes and the Fraunhofer SD up to 1.2 μm. Circles correspond to the measurements that are presented together with their error bars. Computations and measurements have been performed at 647 nm.

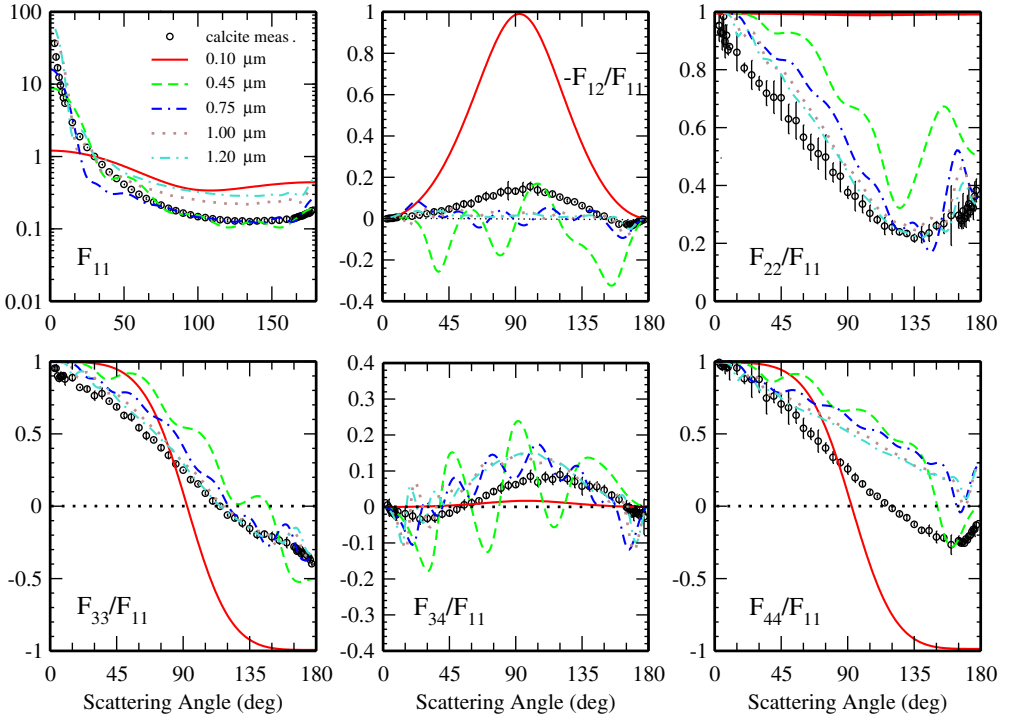

Fig. 9. Computed scattering matrix elements for different volume-equivalent radii. The results are averaged over five rhomboid-like shapes fixing the refractive index to $m_1 = 1.655 + 0.0i$. Circles correspond to the measurements that are presented together with their error bars. Computations and measurements have been performed at 647 nm.

In Fig. 10, we present the scattering matrix elements for the four considered compositions averaged over the five irregular rhomboids. The computations are averaged over the Fraunhofer SD truncated at 1.2 μm. As shown, the $F_{11}(\theta)$ element computed for the isotropic case 2 ($m_2 = 1.485 + 0i$) shows significant differences when compared to the computed values for cases 1, 3, and 4. The computed $F_{11}(\theta)$ shows very similar results for the isotropic cases 1 and 3, and those obtained for birefringent rhomboidal particles, case 4. Therefore, it seems that birefringence has little impact on the computed $F_{11}(\theta)$. Moreover, the $-F_{12}(\theta)/F_{11}(\theta)$ ratio for the "1/3–2/3 approximation" seems to be a good approximation for the birefringent case. The other polarization-related elements show a significant dependence on birefringence.

In general the computed scattering for the birefringent case (4) agrees better with the measured values than the other three studied cases. The only exception is related to the $-F_{12}(\theta)/F_{11}(\theta)$ ratio for which the isotropic refractive index $m_2 = 1.485 + 0.0i$ produces an excellent fit to the measured $-F_{12}(\theta)/F_{11}(\theta)$ from 3 to 95° scattering angle.

4.5. Combination of flake-like and rhomboid-like particles

In this section we study the effect of particle shape on the scattering matrix by comparing the computed scattering matrix elements for flakes and rhomboid-like particles. For simplicity, we only consider size-average results. Further, we only consider the birefringent case. The results of the comparison are shown in Fig. 11 for the Fraunhofer SD. It is clear that all calculated scattering matrix elements are significantly affected by the shape of the particles. When we compare, e.g. the $-F_{12}(\theta)/F_{11}(\theta)$ ratio for both types of shapes we see the change from the bell shape in the case of flakes to a negative branch at large scattering angles, typical for cubes. At this point it is interesting to see whether this behavior would be different by considering the Mie SD. In Fig. 12 we compare the computed scattering matrix elements for flakes and rhomboids averaged over the Mie SD truncated at 1.2 μm. Again, all calculated scattering matrix elements are significantly affected by the shape of the particles. It is important to note that the computed $F_{11}(\theta)$, $F_{22}(\theta)/F_{11}(\theta)$, $F_{33}(\theta)/F_{11}(\theta)$, and $F_{34}(\theta)/F_{11}(\theta)$ for rhomboid-like particles averaged over the Mie SD produce nearly perfect fits to the measurements. Moreover, the measured $-F_{12}(\theta)/F_{11}(\theta)$ ratio presents values within the domains defined by the computed $-F_{12}(\theta)/F_{11}(\theta)$ for flakes and rhomboid-like particles. That is also the case for the calculated $-F_{12}(\theta)/F_{11}(\theta)$, $F_{33}(\theta)/F_{11}(\theta)$, $F_{34}(\theta)/F_{11}(\theta)$, $F_{44}(\theta)/F_{11}(\theta)$ ratios for flakes and rhomboid-like particles averaged over the Fraunhofer SD at nearly the complete scattering angle range. This seems to indicate that a combination of flake- and rhomboid-like particles could provide better fits with the measurements than either shape on its own, consistent with the presence of both types of shapes in the sample.

As illustrative examples, we have computed the scattering matrix considering a varying percentage of flakes and rhomboid-like particles. Fig. 13 presents the results obtained for three different mixtures, namely 80% of flakes and 20% of irregular rhomboids; 50% of flakes and

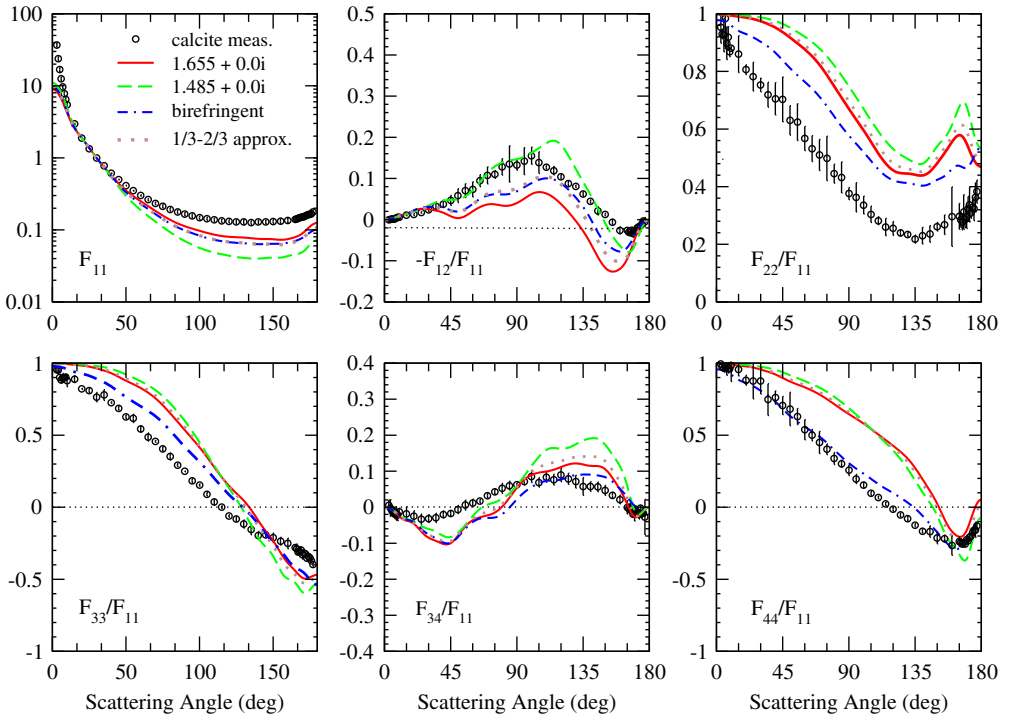

Fig. 10. Computed scattering matrix elements for different refractive indices. The results are averaged over five rhomboid-like shapes and the Fraunhofer SD up to 1.2 μm. Circles correspond to the measurements that are presented together with their error bars. Computations and measurements have been performed at 647 nm.

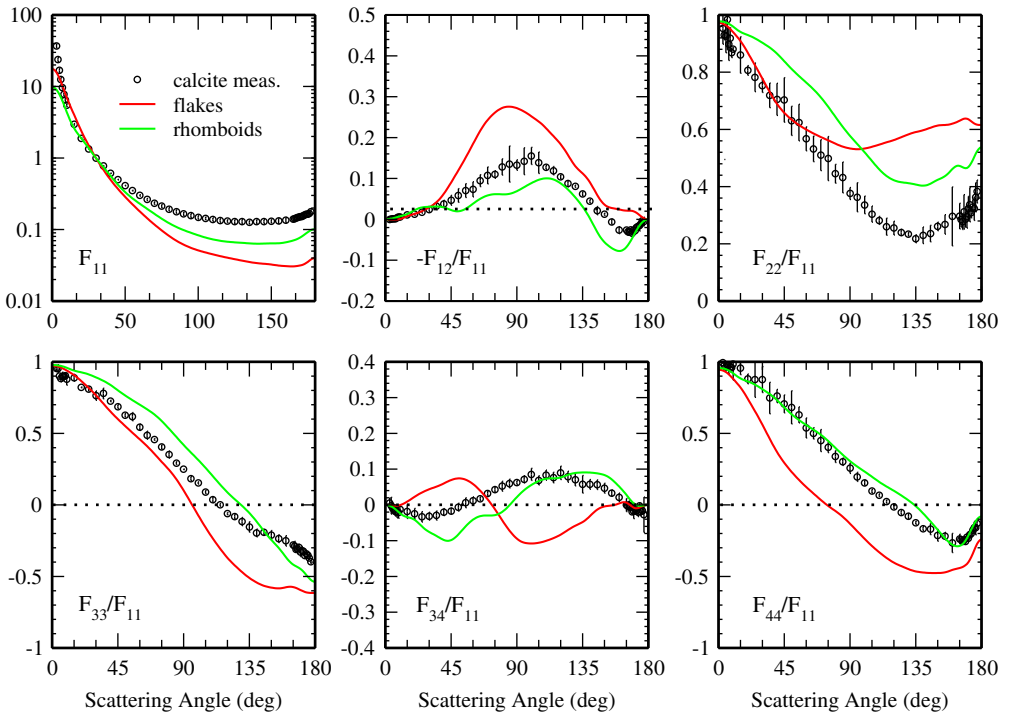

Fig. 11. Computed scattering matrix elements for birefringent flake- and rhomboid-like particles. The results are averaged over shapes and the Fraunhofer SD up to 1.2 μm. Circles correspond to the measurements that are presented together with their error bars. Computations and measurements have been performed at 647 nm.

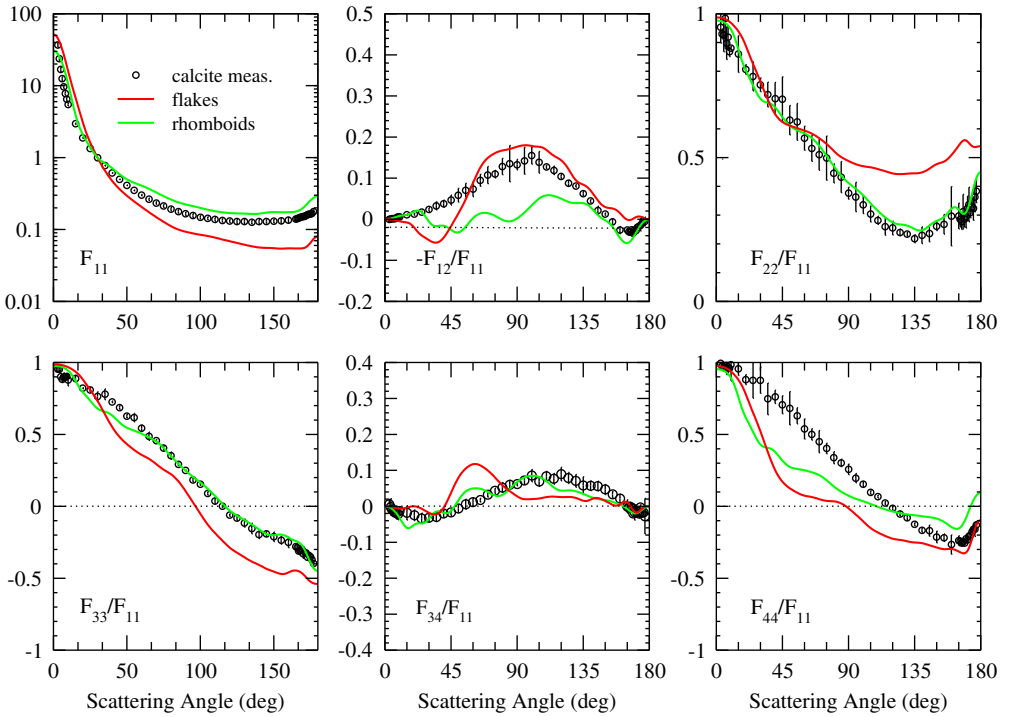

Fig. 12. Computed scattering matrix elements for birefringent flake- and rhomboid-like particles. The results are averaged over shapes and the Mie SD up to 1.2 μm. Circles correspond to the measurements that are presented together with their error bars. Computations and measurements have been performed at 647 nm.

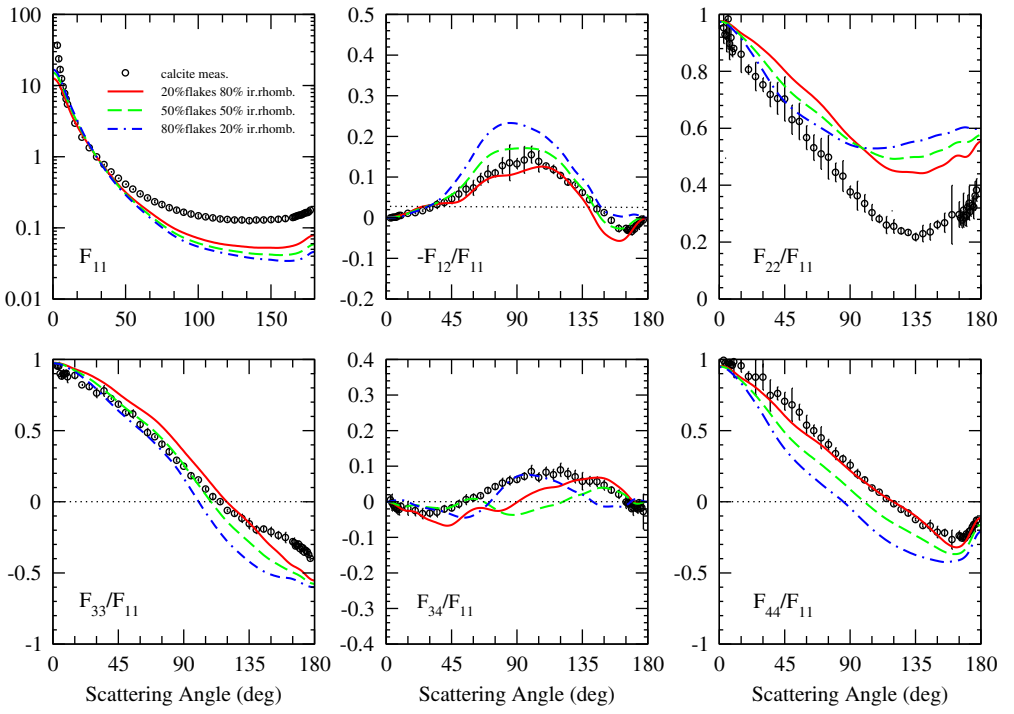

Fig. 13. Computed scattering matrix elements for different percentages of birefringent flake- and rhomboid-like particles. The results are averaged over shapes and the Fraunhofer SD up to 1.2 μm. Circles correspond to the measurements that are presented together with their error bars. Computations and measurements have been performed at 647 nm.

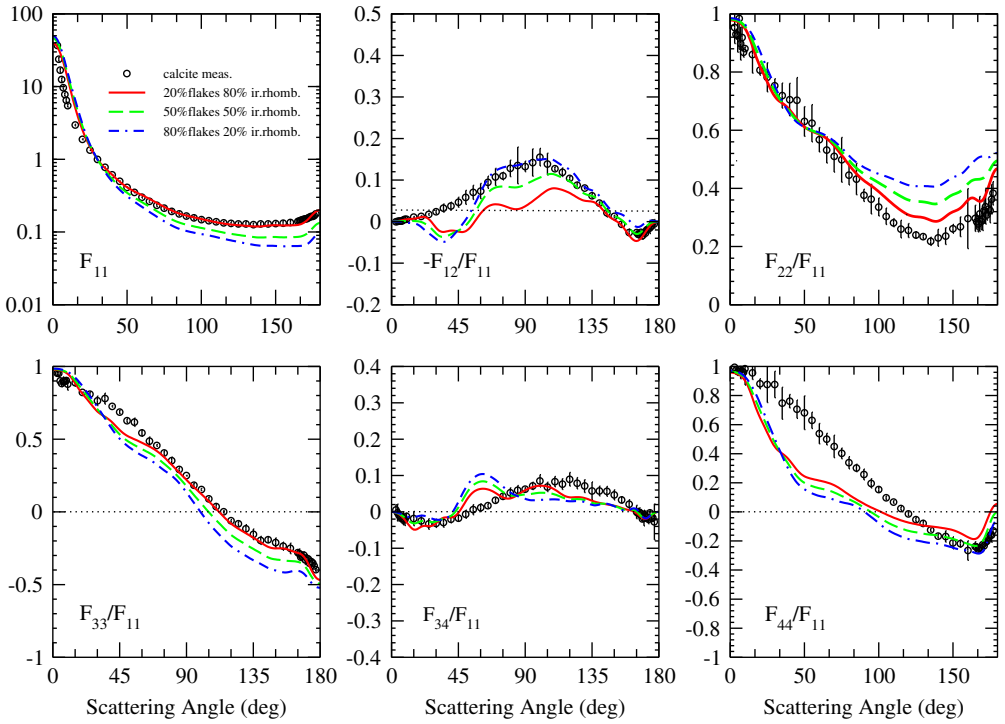

Fig. 14. Computed scattering matrix elements for different percentage of birefringent flake- and rhomboid-like particles. The results are averaged over shapes and the Mie SD up to 1.2 μm. Circles correspond to the measurements that are presented together with their error bars. Computations and measurements have been performed at 647 nm.

50% of irregular rhomboids; and 20% of flakes and 80% of irregular rhomboids. All computations correspond to the birefringent case (4) averaged over the Fraunhofer SD. As shown in the figure, a better agreement with the measurements is reached with those mixtures. In Fig. 14, we present the computed scattering matrix elements for the same three mixtures of flakes and rhomboids just mentioned but averaged over the Mie SD. As shown, a good approximation to the measured scattering matrix elements is also obtained. In the case of the Fraunhofer SD (Fig. 13) a combination of 20% of flakes and 80% of rhomboids give the closest approach to the measurements. That is also the case for Mie SD with the exception of the $-F_{12}(\theta)/F_{11}(\theta)$ ratio which is better represented by the 80% of flakes and 20% rhomboids combination. It is remarkable how similar the computed $F_{11}(\theta)$, $F_{22}(\theta)/F_{11}(\theta)$ and $F_{33}(\theta)/F_{11}(\theta)$ by assuming the Mie SD and a mixture of 20% flakes to 80% rhomboids are the measured ones. Moreover, reasonably good fits are obtained for the $-F_{12}(\theta)/F_{11}(\theta)$ and $F_{44}(\theta)/F_{11}(\theta)$ ratios by assuming the Fraunhofer SD. This seems to indicate that a kind of averaged size distribution out of the Fraunhofer and Mie SDs could give a more adequate representation of the measured scattering matrix elements. In any case, we must point out that the mandatory truncation of the size distributions in the computations prevents us from knowing the effect of larger sized particles. The best fit to the measurements which is found for the 20% flakes to 80% rhomboids combination might change by the inclusion of such particles.

5. Summary and conclusions

In this work, we present the experimental scattering matrix as a function of the scattering angle of a calcite sample. The measurements are performed in the 3–177° scattering angle range. To facilitate the use of the measured scattering matrix of the sample for multiple scattering computations we also present a synthetic scattering matrix based on the measured scattering matrix covering the full angle range from 0 to 180°. The measured and synthetic scattering matrices for the calcite sample are available in the Amsterdam–Granada Light Scattering database at www.iaa.es/scattering. They are freely available under request of citation of this paper and [20].

Since calcite is a birefringent material, the measurements for the calcite sample are used to test the effect of birefringence on the computed scattering matrix elements. We present single scattering computations that have been performed using DDSCAT 7.1 [16]. In our computations, four cases are considered: (1) calcite is considered an isotropic material with refractive index $m_1 = 1.655 + 0.0i$, corresponding to the ordinary refractive index of calcite; (2) calcite is considered an isotropic material with refractive index $m_2 = 1.485 + 0.0i$, corresponding to the extraordinary refractive index of calcite; (3) the "1/3–2/3 approximation" [29], where calcite is considered a mixture of particles such that 1/3 are isotropic particles with refractive index m_2, and 2/3 of the particles with refractive index m_1; (4) the birefringence of calcite is fully accounted for by replacing the

refractive index by a dielectric tensor. All computations are performed at 647 nm. For each of the four mentioned cases, 14 sizes from 0.1 μm to 1.2 μm with a number of orientations ranging from 512 to 1728, are considered. In addition, the scattering matrix elements are modeled for two sets of shapes: flake-like and rhomboid-like particles, giving together 15 different shapes. Due to computational limitations we can only perform computations for particles up to 1.2 μm in radii, i.e. we cannot cover the entire range of sizes of our calcite sample. Therefore, instead of looking for a perfect fitting to the measurements, the experimental scattering matrix is used as qualitative reference to which we can compare our computations to study (a) the effect of birefringence on the computed

Table A1
The synthetic scattering matrix elements obtained with Fraunhofer distribution, as functions of the scattering angle for calcite sample at 647 nm.

Angle (deg)	F_{11}^{au}	$-F_{12}/F_{11}$	F_{22}/F_{11}	F_{33}/F_{11}	F_{34}/F_{11}	F_{44}/F_{11}
0.0	8.61E2	0.00E0	1.00E0	1.00E0	0.00E0	1.00E0
1.0	1.34E2	−3.75E−4	9.93E−1	9.87E−1	2.17E−3	1.00E0
2.0	7.01E1	−9.72E−4	9.75E−1	9.64E−1	5.45E−3	1.00E0
3.0	4.74E1	−1.00E−3	9.53E−1	9.54E−1	5.00E−3	9.94E−1
4.0	5.47E1	0.00E0	9.30E−1	9.53E−1	−2.00E−3	9.74E−1
5.0	3.86E1	1.00E−3	9.26E−1	9.00E−1	−1.00E−2	9.65E−1
6.0	2.87E1	1.00E−3	9.84E−1	8.84E−1	−1.40E−2	9.77E−1
7.0	2.22E1	2.00E−3	8.98E−1	8.97E−1	−1.80E−2	9.78E−1
8.0	1.79E1	4.00E−3	9.80E−1	8.97E−1	−1.80E−2	9.65E−1
9.0	1.49E1	6.00E−3	8.68E−1	9.02E−1	−2.20E−2	9.60E−1
10.0	1.26E1	5.00E−3	8.22E−1	8.78E−1	−1.30E−2	9.84E−1
15.0	6.79E0	1.10E−2	8.60E−1	8.89E−1	−1.80E−2	9.56E−1
20.0	4.33E0	1.20E−2	8.06E−1	8.21E−1	−2.50E−2	8.81E−1
25.0	3.06E0	1.70E−2	7.82E−1	8.10E−1	−3.40E−2	8.75E−1
30.0	2.30E0	2.40E−2	7.53E−1	7.64E−1	−3.20E−2	8.76E−1
35.0	1.78E0	3.30E−2	7.19E−1	7.79E−1	−3.00E−2	7.47E−1
40.0	1.40E0	3.80E−2	7.05E−1	7.26E−1	−2.00E−2	7.61E−1
45.0	1.14E0	4.70E−2	7.03E−1	6.87E−1	−1.70E−2	7.06E−1
50.0	9.46E−1	5.80E−2	6.30E−1	6.27E−1	−6.00E−3	6.82E−1
55.0	8.02E−1	7.00E−2	6.24E−1	6.17E−1	6.00E−3	6.29E−1
60.0	6.91E−1	7.30E−2	5.67E−1	5.43E−1	1.20E−2	5.38E−1
65.0	6.04E−1	9.50E−2	5.32E−1	4.87E−1	1.70E−2	5.00E−1
70.0	5.37E−1	1.07E−1	5.10E−1	4.57E−1	3.20E−2	4.50E−1
75.0	4.89E−1	1.10E−1	4.98E−1	4.04E−1	4.30E−2	4.02E−1
80.0	4.43E−1	1.28E−1	4.45E−1	3.52E−1	5.20E−2	3.38E−1
85.0	4.09E−1	1.35E−1	4.32E−1	2.92E−1	6.00E−2	3.02E−1
90.0	3.81E−1	1.33E−1	3.76E−1	2.49E−1	6.20E−2	2.57E−1
95.0	3.58E−1	1.42E−1	3.63E−1	1.84E−1	7.20E−2	1.96E−1
100.0	3.40E−1	1.55E−1	3.36E−1	1.54E−1	8.50E−2	1.54E−1
105.0	3.28E−1	1.39E−1	3.04E−1	9.00E−2	6.90E−2	9.60E−2
110.0	3.17E−1	1.27E−1	2.82E−1	3.60E−2	8.30E−2	6.80E−2
115.0	3.08E−1	1.19E−1	2.60E−1	0.00E0	7.60E−2	2.30E−2
120.0	3.01E−1	1.04E−1	2.55E−1	−6.10E−2	9.00E−2	−1.50E−2
125.0	2.96E−1	8.70E−2	2.40E−1	−8.20E−2	7.90E−2	−5.30E−2
130.0	2.96E−1	8.10E−2	2.34E−1	−1.16E−1	7.10E−2	−7.90E−2
135.0	2.89E−1	6.20E−2	2.18E−1	−1.54E−1	5.80E−2	−1.25E−1
140.0	2.96E−1	4.40E−2	2.30E−1	−1.96E−1	5.70E−2	−1.66E−1
145.0	2.96E−1	2.10E−2	2.36E−1	−1.92E−1	5.60E−2	−1.69E−1
150.0	3.01E−1	1.20E−2	2.61E−1	−2.12E−1	4.70E−2	−2.13E−1
155.0	3.03E−1	−6.00E−3	2.68E−1	−2.36E−1	3.30E−2	−2.18E−1
160.0	3.12E−1	−2.60E−2	2.96E−1	−2.51E−1	2.10E−2	−2.66E−1
165.0	3.22E−1	−2.60E−2	2.97E−1	−2.80E−1	−0.00E0	−2.39E−1
166.0	3.24E−1	−3.10E−2	2.85E−1	−2.87E−1	−3.00E−3	−2.44E−1
167.0	3.31E−1	−3.10E−2	2.78E−1	−3.11E−1	−1.00E−3	−2.55E−1
168.0	3.38E−1	−2.60E−2	3.12E−1	−3.08E−1	−4.00E−3	−2.46E−1
169.0	3.42E−1	−3.40E−2	2.86E−1	−2.97E−1	−2.00E−2	−2.56E−1
170.0	3.47E−1	−2.60E−2	2.95E−1	−3.29E−1	−1.70E−2	−2.26E−1
171.0	3.49E−1	−2.80E−2	3.23E−1	−3.20E−1	−1.20E−2	−2.33E−1
172.0	3.58E−1	−1.90E−2	3.37E−1	−3.23E−1	−1.50E−2	−2.08E−1
173.0	3.68E−1	−1.70E−2	3.09E−1	−3.55E−1	−2.00E−2	−2.01E−1
174.0	3.77E−1	−1.50E−2	3.29E−1	−3.42E−1	−3.00E−3	−1.76E−1
175.0	3.77E−1	−1.10E−2	3.23E−1	−3.52E−1	−1.80E−2	−1.60E−1
176.0	3.84E−1	−3.00E−3	3.63E−1	−3.71E−1	−1.70E−2	−1.60E−1
177.0	4.09E−1	−5.00E−3	3.83E−1	−3.97E−1	−2.80E−2	−1.30E−1
178.0	4.43E−1	−4.98E−3	4.06E−1	−4.21E−1	−2.42E−2	−3.92E−2
179.0	4.72E−1	−1.94E−3	4.31E−1	−4.37E−1	−8.98E−3	6.45E−2
180.0	4.85E−1	0.00E0	4.43E−1	−4.43E−1	0.00E0	1.14E−1

scattering matrix elements and (b) the validity of our shape models to reproduce the scattering behavior of our calcite sample.

First, we analyze the effect of birefringence on the computed scattering matrix elements. In general, the simulated scattering matrices show a strong dependence on the particle sizes. For both flakes and irregular rhomboids, we have found that the isotropic cases 1 ($m_1 = 1.655$) and 3 (1/3–2/3 approximation), provide quite similar values for the $F_{11}(\theta)$ element to those obtained

Table A2
The synthetic scattering matrix elements obtained with Mie size distribution, as functions of the scattering angle for calcite sample at 647 nm.

Angle (deg)	F_{11}^{au}	$-F_{12}/F_{11}$	F_{22}/F_{11}	F_{33}/F_{11}	F_{34}/F_{11}	F_{44}/F_{11}
0.0	2.68E3	0.00E0	1.00E0	1.00E0	0.00E0	1.00E0
1.0	3.28E2	−3.75E−4	9.93E−1	9.87E−1	2.17E−3	1.00E0
2.0	1.55E2	−9.72E−4	9.75E−1	9.64E−1	5.45E−3	1.00E0
3.0	9.56E1	−1.00E−3	9.53E−1	9.54E−1	5.00E−3	9.94E−1
4.0	5.03E1	0.00E0	9.30E−1	9.53E−1	−2.00E−3	9.74E−1
5.0	3.55E1	1.00E−3	9.26E−1	9.00E−1	−1.00E−2	9.65E−1
6.0	2.63E1	1.00E−3	9.84E−1	8.84E−1	−1.40E−2	9.77E−1
7.0	2.05E1	2.00E−3	8.98E−1	8.97E−1	−1.80E−2	9.78E−1
8.0	1.65E1	4.00E−3	9.80E−1	8.97E−1	−1.80E−2	9.65E−1
9.0	1.37E1	6.00E−3	8.68E−1	9.02E−1	−2.20E−2	9.60E−1
10.0	1.16E1	5.00E−3	8.22E−1	8.78E−1	−1.30E−2	9.84E−1
15.0	6.24E0	1.10E−2	8.60E−1	8.89E−1	−1.80E−2	9.56E−1
20.0	3.98E0	1.20E−2	8.06E−1	8.21E−1	−2.50E−2	8.81E−1
25.0	2.82E0	1.70E−2	7.82E−1	8.10E−1	−3.40E−2	8.75E−1
30.0	2.11E0	2.40E−2	7.53E−1	7.64E−1	−3.20E−2	8.76E−1
35.0	1.63E0	3.30E−2	7.19E−1	7.79E−1	−3.00E−2	7.47E−1
40.0	1.29E0	3.80E−2	7.05E−1	7.26E−1	−2.00E−2	7.61E−1
45.0	1.05E0	4.70E−2	7.03E−1	6.87E−1	−1.70E−2	7.06E−1
50.0	8.70E−1	5.80E−2	6.30E−1	6.27E−1	−6.00E−3	6.82E−1
55.0	7.37E−1	7.00E−2	6.24E−1	6.17E−1	6.00E−3	6.29E−1
60.0	6.36E−1	7.30E−2	5.67E−1	5.43E−1	1.20E−2	5.38E−1
65.0	5.55E−1	9.50E−2	5.32E−1	4.87E−1	1.70E−2	5.00E−1
70.0	4.94E−1	1.07E−1	5.10E−1	4.57E−1	3.20E−2	4.50E−1
75.0	4.50E−1	1.10E−1	4.98E−1	4.04E−1	4.30E−2	4.02E−1
80.0	4.08E−1	1.28E−1	4.45E−1	3.52E−1	5.20E−2	3.38E−1
85.0	3.76E−1	1.35E−1	4.32E−1	2.92E−1	6.00E−2	3.02E−1
90.0	3.51E−1	1.33E−1	3.76E−1	2.49E−1	6.20E−2	2.57E−1
95.0	3.29E−1	1.42E−1	3.63E−1	1.84E−1	7.20E−2	1.96E−1
100.0	3.13E−1	1.55E−1	3.36E−1	1.54E−1	8.50E−2	1.54E−1
105.0	3.02E−1	1.39E−1	3.04E−1	9.00E−2	6.90E−2	9.60E−2
110.0	2.91E−1	1.27E−1	2.82E−1	3.60E−2	8.30E−2	6.80E−2
115.0	2.83E−1	1.19E−1	2.60E−1	0.00E0	7.60E−2	2.30E−2
120.0	2.77E−1	1.04E−1	2.55E−1	−6.10E−2	9.00E−2	−1.50E−2
125.0	2.72E−1	8.70E−2	2.40E−1	−8.20E−2	7.90E−2	−5.30E−2
130.0	2.72E−1	8.10E−2	2.34E−1	−1.16E−1	7.10E−2	−7.90E−2
135.0	2.66E−1	6.20E−2	2.18E−1	−1.54E−1	5.80E−2	−1.25E−1
140.0	2.72E−1	4.40E−2	2.30E−1	−1.96E−1	5.70E−2	−1.66E−1
145.0	2.72E−1	2.10E−2	2.36E−1	−1.92E−1	5.60E−2	−1.69E−1
150.0	2.77E−1	1.20E−2	2.61E−1	−2.12E−1	4.70E−2	−2.13E−1
155.0	2.79E−1	−6.00E−3	2.68E−1	−2.36E−1	3.30E−2	−2.18E−1
160.0	2.87E−1	−2.60E−2	2.96E−1	−2.51E−1	2.10E−2	−2.66E−1
165.0	2.96E−1	−2.60E−2	2.97E−1	−2.80E−1	−0.00E0	−2.39E−1
166.0	2.98E−1	−3.10E−2	2.85E−1	−2.87E−1	−3.00E−3	−2.44E−1
167.0	3.04E−1	−3.10E−2	2.78E−1	−3.11E−1	−1.00E−3	−2.55E−1
168.0	3.10E−1	−2.60E−2	3.12E−1	−3.08E−1	−4.00E−3	−2.46E−1
169.0	3.15E−1	−3.40E−2	2.86E−1	−2.97E−1	−2.00E−2	−2.56E−1
170.0	3.19E−1	−2.60E−2	2.95E−1	−3.29E−1	−1.70E−2	−2.26E−1
171.0	3.21E−1	−2.80E−2	3.23E−1	−3.20E−1	−1.20E−2	−2.33E−1
172.0	3.29E−1	−1.90E−2	3.37E−1	−3.23E−1	−1.50E−2	−2.08E−1
173.0	3.38E−1	−1.70E−2	3.09E−1	−3.55E−1	−2.00E−2	−2.01E−1
174.0	3.46E−1	−1.50E−2	3.29E−1	−3.42E−1	−3.00E−3	−1.76E−1
175.0	3.46E−1	−1.10E−2	3.23E−1	−3.52E−1	−1.80E−2	−1.60E−1
176.0	3.53E−1	−3.00E−3	3.63E−1	−3.71E−1	−1.70E−2	−1.60E−1
177.0	3.76E−1	−5.00E−3	3.83E−1	−3.97E−1	−2.80E−2	−1.30E−1
178.0	4.07E−1	−4.98E−3	4.06E−1	−4.21E−1	−2.42E−2	−3.92E−2
179.0	4.34E−1	−1.94E−3	4.31E−1	−4.37E−1	−8.98E−3	6.45E−2
180.0	4.46E−1	0.00E0	4.43E−1	−4.43E−1	0.00E0	1.14E−1

by assuming birefringent particles (case 4). Therefore, for the studied shapes and sizes, birefringence has little impact on the computed phase functions. In contrast, birefringence produces a significant effect on the polarization-related scattering matrix elements. The obtained conclusions are in agreement with [15]. In the case of flakes, the isotropic refractive index m_1 provides a good approximation to the birefringent case for the $-F_{12}(\theta)/F_{11}(\theta)$ ratio. In contrast, for irregular rhomboids, the "1/3-2/3" approximation provides closest values to the computed $-F_{12}(\theta)/F_{11}(\theta)$ for birefringent particles.

Second, the simulations are compared with the experimental scattering matrix for the calcite sample. It is interesting to note that the shape of the targets (flakes or irregular rhomboids) has a much stronger effect on the computed scattering matrix elements than the birefringence. Significant differences in the simulated scattering matrices are found between those two types of particles. Since our sample consists of two types of particles, we compare the matrices obtained for different percentages of flakes and irregular rhomboids.

We find that varying the percentage of flakes and irregular rhomboids in the sample, we get a significantly better approximation to the measurements than for flakes or irregular rhomboids alone. For the Fraunhofer SD computations, we find that a particle shape distribution having 20% of flakes and 80% of irregular rhomboids gives a better approximation to the measurements. The agreement with the measurements is even better in the case of the Mie SD even considering that the calculated cross section in the former case is 74% of the total scattering cross-section while in the Mie SD it is only 55%. That is probably due to the fact that the resulting r_{eff} of the Mie SD after the truncation at 1.2 μm is closer to the r_{eff} of any of the two size distributions (Mie and Fraunhofer) before truncation. The limitations of the computations due to the extreme difficulties in dealing with large particle sizes prevent us from drawing firm conclusions on the relative percentages of different particle shapes that exist in the calcite sample. We hope, however, that further computations including particles in geometric optics domain will shed more light on the issue.

Acknowledgments

J.R. Rodon and A. Benitez from IAA GRID team are heartily acknowledged for their support. Furthermore we are indebted to A. Gonzalez and I. Guerra Tschuschke from The Scientific Instrumentation Center of the University of Granada, who took the FESEM and SEM images of the calcite samples. Bob West and two anonymous referee are acknowledged by their reviews on a previous version of this paper. This work has been supported by the Plan Nacional de Astronomia y Astrofisica under Contract AYA2009-08190 and Junta de Andalucia under Contract P09-FMQ-455. Timo Nousiainen and Evgenij Zubko acknowledge the Academy of Finland (Contracts 125180 and 127461) for its financial support. Evgenij Zubko also acknowledges NASA program for Outer Planets Research (Grant NNX10AP93G).

Appendix A

Synthetic scattering matrix elements as functions of the scattering angle by assuming the Fraunhofer SD A1 and the Mie SD A2.

References

[1] Abergel A, Ade PAR, Aghanim N, Arnaud M, Ashdown M, Aumont J, et al. Planck Collaboration. Planck early results. XXIV. Dust in the diffuse interstellar medium and the galactic halo. Astron Astrophys 2011;536:A24.
[2] Kirk H, Johnstone D, Di Francesco J. The large- and small-scale structures of dust in the star-forming perseus molecular cloud. Astrophys J 2006;646:1009–23.
[3] Weingartner JC, Draine BT. Dust grain-size distributions and extinction in the milky way, large magellanic cloud, and small magellanic cloud. Astrophys J 2001;548:296–309.
[4] Moreno F, Lara ML, Muñoz O, López-Moreno JJ, Molina A. Dust in comet 67P/Churyumov–Gerasimenko. Astrophys J 2004;613:1263–9.
[5] Mishchenko MI, Travis LD, Lacis AA. Scattering, absorption, and emission of light by small particles. Cambridge University Press; 2002.
[6] Nousiainen T. Optical modeling of mineral dust particles: a review. J Quant Spectrosc Radiat Transfer 2009;110:1261–79.
[7] Pollack JB, Colburn DS, Flasar FM, Kahn R, Carlston CE, Pidek DG. Properties and effects of dust particles suspended in the martian atmosphere. J Geophys Res 1979;84:2929–45.
[8] Marchiori E, Lourenço S, Davaus Gasperetto T, Zanetti G, Mauro Mano LF, Nobre LF. Pulmonary talcosis: imaging findings. Lung 2010;188:165–71.
[9] Muñoz O, Volten H, Hovenier JW, Nousiainen T, Muinonen K, Guirado D, et al. Scattering matrix of large saharan dust particles: experiments and computations. J Geophys Res D 2007;112:D13215.
[10] Liu L, Mishchenko MI, Hovenier JW, Volten H, Muñoz O. Scattering matrix of quartz aerosols: comparison and synthesis of laboratory and Lorentz–Mie results. J Quant Spectrosc Radiat Transfer 2003;79–80:911–20.
[11] Kahnert M, Nousiainen T. Uncertainties in measured and modeled asymmetry parameters of mineral dust aerosol. J Quant Spectrosc Radiat Transfer 2006;100:173–8.
[12] Booth MC, Kieffer HH. Carbonate formation in Mars-like environments. J Geophys Res 1978;83:1809–15.
[13] Gooding JL. Chemical weathering on Mars. Thermodynamic stabilities of primary minerals (and their alteration products) from mafic igneous rocks. Icarus 1978;33:483–513.
[14] Claquin T, Schultz M, Balkanski Y. Modeling the mineralogy of atmospheric dust sources. J Geophys Res 1999;104(22):243–56.
[15] Nousiainen T, Zubko E, Nieminen JV, Kupiainen K, Lehtinen, Muinonen K, et al. Single scattering modeling of thin, birefringent mineral dust flakes using the discrete dipole approximation. J Geophys Res 2009;114:D07207.
[16] Draine BT. The discrete dipole approximation for light scattering by irregular targets. In: Mishchenko MI, Hovenier JW, Travis LD, editors. Light scattering by nonspherical particles. San Diego, CA: Academic Press; 2000. p. 131.
[17] Orofino V, Blanco A, Fonti S, Proce R, Rotundi A. The infrared optical constants of limestone particles and implications for the search of carbonates on Mars. Planet Space Sci 1998;46(11–12):1659–69.
[18] Muñoz O, Moreno F, Guirado D, Ramos JL, Volten H, Hovenier JW. The IAA cosmic dust laboratory: experimental scattering matrices of clay particles. Icarus 2011;211(1):894–900.
[19] Volten H, Muñoz O, Hovenier JW, de Haan JF, Vassen W, van der Zande WJ, et al. WWW scattering matrix database for small mineral particles at 441.6 and 632.8 nm. J Quant Spectrosc Radiat Transfer 2005;90:191–206.
[20] Muñoz O, Moreno F, Guirado D, Dabrowska DD, Volten H, Hovenier JW. The Amsterdam–Granada light scattering database. J Quant Spectrosc Radiat Transfer 2012;113(7):565–74.
[21] Hansen JE, Travis LD. Light scattering in planetary atmospheres. Space Sci Rev 1974;16:527–610.
[22] Ghosh G. Dispersion-equation coefficients for the refractive index and birefringence of calcite and quartz crystals. Opt Commun 1999;163:95–102.
[23] van de Hulst HC. Light scattering by small particles. NY: John Wiley & Sons, Inc.; 1957 (Also Dover Publications Inc. N.Y., 1981).

[24] Hovenier JW, van der Mee CVM, Domke H. Transfer of polarized light in planetary atmospheres: basic concepts and practical methods. Dordrecht: Kluwer, Springer; 2004.
[25] Muñoz O, Moreno F, Guirado D, Ramos JL, López A, Girela F, et al. Experimental determination of scattering matrices of dust particles at visible wavelengths: the IAA light scattering apparatus. J Quant Spectrosc Radiat Transfer 2010;111:187–96.
[26] Hovenier JW. Measuring scattering matrices of small particles at optical wavelengths. In: Mishchenko MI, Hovenier JW, Travis LD, editors. Light scattering by nonspherical particles. San Diego, CA: Academic Press; 2000. p. 355–65.
[27] Hovenier JW, van de Hulst HC, van der Mee CVM. Conditions for the elements of the scattering matrix. Astron Astrophys 1986;157:301–10.
[28] Volten H, Muñoz O, Hovenier JW, Waters LBFM. An update of the Amsterdam light scattering database. J Quant Spectrosc Radiat Transfer 2006;100:437–43.
[29] Draine BT. The discrete dipole approximation and its application to interstellar graphite grains. Astrophys J 1988;333:848–72.
[30] Zubko E, Petrov D, Grynko Y, Shkuratov, Okamoto H, Muinonen K, et al. Validity criteria of the discrete dipole approximation. Appl Opt 2010;49(8):1267–79.
[31] Dabrowska DD, Muñoz O, Moreno F, Nousiainen T, Zubko E. The effect of the orientation of the optic axis on simulated scattering matrix elements of small birefringent particles. Opt Lett 2012;37(15): 3252–4.